Spatial and Spectral Analysis and Modeling of Transversal Chromatic Aberrations and their Compensation

Julie Klein, Johannes Brauers and Til Aach; Institute of Imaging and Computer Vision, RWTH Aachen University; D-52056 Aachen, Germany

Abstract

The wavelength-dependency of the refraction indices in optical systems involves chromatic aberrations: one object point is not projected on exactly one image point on the sensor plane, but dispersed depending on its wavelengths in a rainbow-like manner due to the wavelength-dependency. These distortions have already been analyzed for the three broadband color planes red, green and blue of an RGB camera for example. As far as the authors know, no analysis was performed yet for more than three narrow wavelength bands and each color plane was considered separately so far.

In this paper, we describe the measurement of chromatic aberrations for multiple narrowband color channels and extend the models from the literature to characterize these distortions. We then link the parameters obtained for all color channels in order to include the wavelength-dependency into the models of the distortions. This leads to a more general model for the chromatic aberrations, calculating the distortions as a function of the wavelength and the image position. We then compensate the chromatic aberrations using these models and finally estimate their accuracy.

Introduction

Chromatic aberrations are present in nearly every imaging system. They are caused by the wavelength-dependent indices of refraction of glasses which are used in a lens. The different wavelengths reemitted by an object point do not focus exactly on the same point and thus arrive at the sensor plane at different positions, which results in different image points for this one object point. There are two categories of chromatic aberrations: the longitudinal chromatic aberrations and the transversal chromatic aberrations [1]. The longitudinal ones result from the variation of the focus along the optical axis and cause blurring; the transversal ones result from the displacement of the image points in the sensor plane and cause color fringes [2]. In this work, we analyze the transversal chromatic aberrations.

Models and compensation of chromatic aberrations are important for every optical system dealing with colors and in particular for the multispectral imaging. Several types of multispectral cameras use optical bandpass filters to divide the electromagnetic spectrum into different passbands. Research groups use five to thirteen bandpass filters [3, 4, 5, 6, 7, 8, 9]. The five to thirteen different spectral filters give as many grayscale images corresponding to the wavelength bands of the filters. These grayscale images have to be combined in order to constitute a multispectral image. We estimate the incident spectra from the grayscale images via Wiener estimation shown in [10, 6] and transform them to an RGB image; other, more sophisticated methods may be used [11]. Because of the chromatic aberrations, the grayscale images are slightly shifted and blurred compared to each other. This causes color fringes when the different color channels, i.e., the different wavelength bands, are combined. The multispec-

tral systems also encounter other aberrations, like the filter aberrations discussed in [10]. Analyzing the aberrations separately allows better models and better compensation, and thus a better output image.

In prior work, the chromatic aberrations were measured over the whole image. In [12], beads are stained with three different narrowband fluorescent dyes simultaneously and the chromatic aberrations are measured using their weight centers. In [13, 14, 15], the measurements were performed using edges of a pattern with known geometry that are detected on three broadband color planes (the color planes red, green and blue of the RGB cameras). In [16], the three color planes of an RGB camera were also used, but the detected edges were the crossings of a checkerboard pattern. Our approach generalizes this by detecting the crossings of a checkerboard pattern on seven different narrowband color channels. The effect of the chromatic aberrations can thus be analyzed in a more precise way than with the three broadband color channels red, green and blue or than with only three narrowband color channels from the fluorescent microscopy.

Some models describing the chromatic aberrations are introduced in the literature: The horizontal and vertical components of the lateral chromatic aberrations depend almost linearly on the position of the image point in [12]. In [13], the displacements between the images of two color planes were fitted with a cubic spline, separately for the two coordinates of the image. In [14], a radial correction was computed in order to align the edges in the red and blue planes to the edges in the green plane. The radial and decentering distortion from [17] was used in [16], where the distortion of an image point from a color plane (e.g., for the red or the blue color plane) was calculated as a function of the corresponding image point from the reference color plane (e.g., for the green color plane). Another model could be an affine model, in which the displacement of the image point between two color planes is described by a rotation, a translation and a scaling [10].

All these models describe relative distortions, since the position of the image point without any chromatic aberration is not available. Up to now, the chromatic aberrations of each color channel were analyzed separately and no link between the channels was given. Therefore, we analyze here the chromatic aberrations as a function of the wavelength and the image position and derive a more general model.

In this work, we first describe the experimental setup used to measure the chromatic aberrations and the observations for the seven different color channels. We then establish models for the distortions of the points of interest and we explain how these distortions are compensated. In the fourth section, we give detailed results of our analysis and deduce a new model for the chromatic aberrations, incorporating the wavelength of the observed color plane. Finally, we conclude the paper with a discussion.

Physical Background

Each object point is displayed on the sensor plane through the objective. Since the indices of refraction of the optical elements are wavelength-dependent, the object point is split into its spectral components and is thus spread over a rainbow-like cloud of image points. For example, the blue wavelength band is more strongly refracted than the red one [18] and in our images, the image points corresponding to the blue wavelengths are nearer to the optical axis than those corresponding to the red wavelengths. This results in color fringes at the edges in the image, as shown in Fig. 1.

Figure 1. *Chromatic aberrations on the bottom left corner of the image of a checkerboard pattern.*

The object points along the optical axis of the objective are not distorted by the chromatic aberrations: their lines of sight follow the optical axis and all their image points are located on the same point $(u_0, v_0)^T$, which is the point where the optical axis intersects with the sensor plane. The optical axis is free of chromatic aberrations and the point $(u_0, v_0)^T$ of the sensor is the center of the chromatic aberrations.

Experimental Setup

To measure the chromatic aberrations, we observe an object point and locate its corresponding image points for known wavelengths, e.g., for seven wavelength bands spread over the visible spectrum. The object points whose image points have to be followed are the crossings of a checkerboard pattern. We use a checkerboard pattern because its crossings are straightforward to localize. They are detected and their positions are determined with a subpixel accuracy using the algorithm explained in [19]. The crossings can be localized with an accuracy of about 0.03 pixels for images with low noise levels like ours.

To isolate the image points for known wavelengths, we use spectral bandpass filters that enable us to allow only one wavelength band coming from the object point to pass and to hit the sensor. The choice of the place of the filters in the optical path matters strongly. Indeed, when the filters are situated between the object and the sensor, they lead to additional aberrations due to their different indices of refraction and their different thicknesses. These filter aberrations are analyzed in [10]. Such a configuration would prevent the chromatic aberrations from being measured separately from any other aberration. For this reason, we place the spectral filters in front of the light source: the scene is directly illuminated with the wavelength band of interest and only this wavelength band arrives at the optical system. With this experimental setup, each wavelength band is isolated on a different color channel representing the scene. Each object point then is projected to several image points on the sensor plane, depending on the considered wavelength band. The coordinates of the image points are $(u_\lambda, v_\lambda)^T$, with λ the wavelength of the color channel. In the following, we will use the relative coordinates of

the image points $\mathbf{p}_\lambda$ which relate to the center of the distortions $(u_0, v_0)^T$: $\mathbf{p}_\lambda = (x_\lambda, y_\lambda)^T = (u_\lambda - u_0, v_\lambda - v_0)^T$.

The seven spectral filters we use have central wavelengths going from 400 to 700 nm in steps of 50 nm and bandpass widths of 40 nm and are mounted in a filter wheel (see Fig. 2).
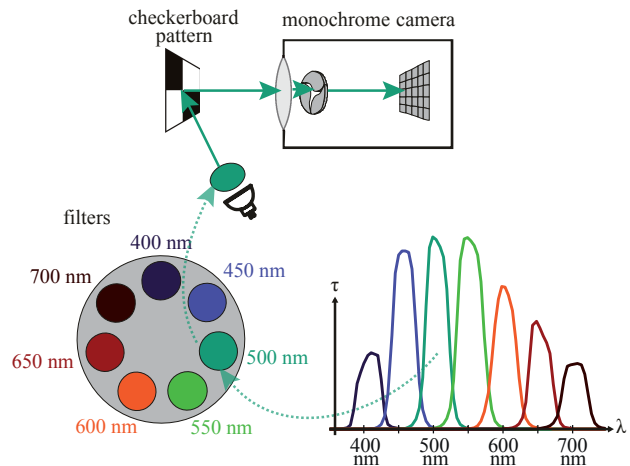

Figure 2. *Experimental setup to measure the chromatic aberrations: a checkerboard pattern is illuminated through a narrowband spectral filter and the scene is recorded by a monochrome camera. The transmission curves of the seven filters that are included in a filter-wheel are displayed.*

Observations

When analyzing the positions of the checkerboard crossings on the acquired checkerboard pattern (see Fig. 3(a)) for different wavelength bands, the wavelength-dependency of the lens can be observed. For increasing wavelengths, the crossings move toward the edges of the image and their displacements exhibit a radial symmetry around the distortion center. It is then reasonable to take one of the outer color channels (i.e. whose central wavelength is the lowest or highest one) as reference channel to consider the distortions. We selected the 700 nm channel as reference and the image was focused manually at the reference wavelength. The vectors from Fig. 3(a) show how the crossings were displaced relative to the crossings of the reference channel, with a 50 × magnification. The vectors of the low wavelengths are longer than those of the high wavelengths. For each crossing, all the displacement vectors relative to the reference channel have approximately the same direction, as shown in Fig. 3(b).

Models for Chromatic Aberrations

To measure and model the chromatic aberrations, we consider a reference color channel r with center wavelength λ_r and another color channel c with center wavelength λ_c. We then analyze the distortions of the checkerboard crossings between the reference color channel and the current color channel. To simplify notation, the image points of the channel r are written $(u_r, v_r)^T$ instead of $(u_{\lambda_r}, v_{\lambda_r})^T$ and the image points of the channel c are written $(u_c, v_c)^T$ instead of $(u_{\lambda_c}, v_{\lambda_c})^T$. Their corresponding relative coordinates are $\mathbf{p}_r = (x_r, y_r)^T = (u_r - u_0, v_r - v_0)^T$ and $\mathbf{p}_c = (x_c, y_c)^T = (u_c - u_0, v_c - v_0)^T$, $(u_0, v_0)^T$ being the center of the chromatic aberrations. The distortions of a color channel are described by the set of vectors $\mathbf{p}_c - \mathbf{p}_r$ for all the crossings of the checkerboard pattern. The vectors describe relative distortions, since the reference channel exhibits chromatic aberrations, too. The aim of this work is to establish a model for these distortions for the whole image and for the wavelengths
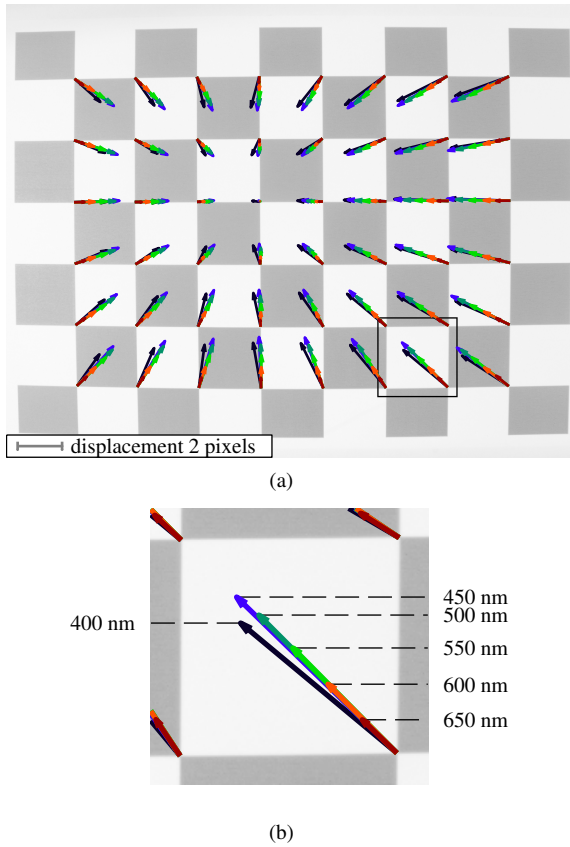
(a)

(b)

Figure 3. *Displacements of the color channels relative to the reference channel (a): for each color channel from 400 nm to 650 nm, the displacements of the crossings to the corresponding crossings in the reference channel 700 nm are displayed with a 50 × magnification. The vectors inside the black frame are displayed in (b). Each color represents one wavelength band.*

of the visible light. In this section, we will derive a few models for the chromatic aberrations and explain how the chromatic aberrations can be compensated.

The chromatic aberrations are first measured on a checkerboard pattern and the parameters of the models are derived. The models can then be applied to other captured images, even if they are situated at different distances from the camera, since the distortions depend only on the angles of the rays arriving at the optical system and not on the object distances.

The objective of each model is to determine an estimate $\hat{\mathbf{p}}_c$ of an image point's position in the current channel, given its position $\mathbf{p_r}$ in the reference channel. We start with elementary affine and radial models for the distortions. We then extend the model to a parametric model which takes both radial and tangential components of the distortions into account, where the model parameters are determined by an optimization procedure. We will show that this model provides high accuracy for the distortions within each given color channel. In a final step, we add another model which describes the above optimized parameters over wavelength, thus enabling us to characterize chromatic aberrations also for wavelengths *between* the color channels.

Affine Model

In this model, it is assumed that the points $\mathbf{p}_r$ and $\mathbf{p}_c$ are related by an affine transformation including a rotation, a translation and a nonisotropic scaling. The estimated image point $\hat{\mathbf{p}}_c^{aff}$

is calculated as follows using the matrix $\mathbf{T}_c \in \mathbb{R}^{2 \times 3}$:

$$\hat{\mathbf{p}}_c^{aff} = \mathbf{T}_c \cdot \begin{pmatrix} \mathbf{p}_r \\ 1 \end{pmatrix}, \tag{1}$$

where the elements $T_c(1,3)$ and $T_c(2,3)$ describe a translation and the other elements describe a rotation and a nonisotropic scaling.

The distortion $\Delta\mathbf{e}_c^{aff} = \hat{\mathbf{p}}_c^{aff} - \mathbf{p}_r$ caused by the chromatic aberrations is then computed by:

$$\Delta\mathbf{e}_c^{aff}(\mathbf{p}_r) = \left(\mathbf{T}_c - \begin{pmatrix} 1 & 0 & 0 \\ 0 & 1 & 0 \end{pmatrix} \right) \cdot \begin{pmatrix} \mathbf{p}_r \\ 1 \end{pmatrix} \tag{2}$$

As shown in the results, this straightforward model compensates some of the distortions, but its approximation errors exceed those of the following models considerably (see Fig. 7). The wavelength-dependency of this model was therefore not further investigated.

Radial Model

A first glance at the displacements of the crossings seems to show that the distortions exhibit only a radial component (see Fig. 3(a)). For this reason, we use a model accounting only the lengths of the distortions with respect to the radii of the crossings. The radius $r_r = \|\mathbf{p}_r\|$ of a crossing refers here to the distance between the crossing of the reference color channel and the center of the aberrations. Figure 4 shows the lengths of the distortions for the crossings of each wavelength band as a function of the radius of the crossings from the reference wavelength band 700 nm. For each crossing of the reference color channel, we determine its radius and we examine how it is distorted in the other color channels and measure the length of this distortion. The relation between radius and lengths of the distortions can be approximated by a third-order polynomial for each color channel.

In the radial model, we assume that $\mathbf{p}_r$ and $\mathbf{p}_c$ are colinear and point in the same direction. We choose the 700 nm channel as reference, consequently $\mathbf{p}_r$ is longer than $\mathbf{p}_c$. The length of $\mathbf{p}_c - \mathbf{p}_r$ is a function $f_c(r_r)$ of $r_r = \|\mathbf{p}_r\|$, as explained previously. These assumptions lead to the following estimation of the distortion $\Delta\mathbf{e}_c^{rad}$:

$$\begin{aligned} \Delta\mathbf{e}_c^{rad}(\mathbf{p}_r) &= \hat{\mathbf{p}}_c^{rad} - \mathbf{p}_r \\ &= -f_c(\|\mathbf{p}_r\|) \frac{\mathbf{p}_r}{\|\mathbf{p}_r\|} \end{aligned} \tag{3}$$

As shown in Fig. 4, the function $f_c(r_r)$ can be approximated by a third-order polynomial:

$$f_c(r_r) \approx l_{c,1} \cdot r_r^3 + l_{c,2} \cdot r_r^2 + l_{c,3} \cdot r_r + l_{c,4}, \tag{4}$$

with specific coefficients $l_{c,i}$, $i = 1, \ldots, 4$, for each color channel c. The values of these coefficients are provided in the results in Tab. 1. For each i, these coefficients describe the chromatic aberrations for the center wavelength λ_c, $\lambda_c \in \{400\text{ nm}, 450\text{ nm}, 500\text{ nm}, 550\text{ nm}, 600\text{ nm}, 650\text{ nm}\}$, of the i-th color channel. We will now show that the *wavelength-dependency* of these coefficients can, in turn, be modelled parametrically, thus allowing to determine chromatic aberrations also for color channels with *other center wavelengths* than the ones above. Towards this end, we describe the wavelength-dependency of the coefficients $l_{c,i}$ by a third-order polynomial with coefficients $m_{i,j}$, $j = 1, \ldots, 4$, as follows:

$$l_{c,i} \approx m_{i,1} \cdot \lambda_c^3 + m_{i,2} \cdot \lambda_c^2 + m_{i,3} \cdot \lambda_c + m_{i,4} \tag{5}$$
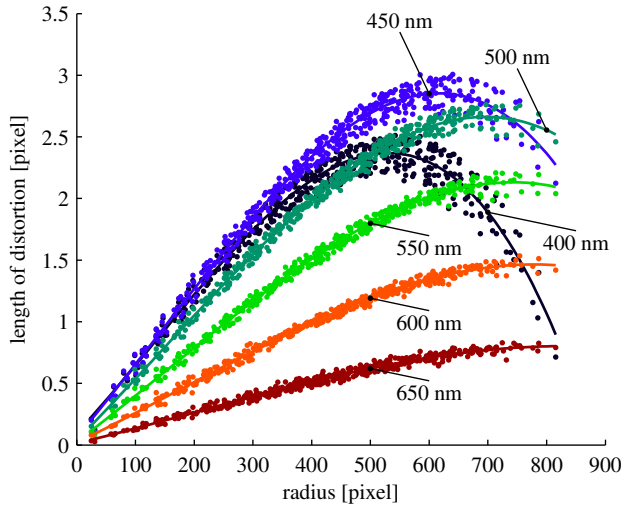
Figure 4. *Lengths of the distortions of the color channels. The dots are the measurements and the lines are polynomials of third-order fitting them (coefficients of the fittings: see Tab. 1).*

By insertion of Eq. (5) in Eq. (4), the length of the distortion $\|\mathbf{p}_c - \mathbf{p}_r\|$ can be expressed as $f(\lambda, r_r)$, a function of the relative position of the crossing $\mathbf{p}_r$ and of the wavelength λ. This generalizes to the whole visible spectrum the function $f_c(r_r)$ that was only defined for the narrowband color channels. The function $f(\lambda, r_r)$ has then 16 coefficients $m_{i,j}$, $i, j = 1, \ldots, 4$:

$$f(\lambda, r_r) = \sum_{i=1}^{4} \sum_{j=1}^{4} m_{i,j} \cdot \lambda^{4-j} \cdot r_r^{4-i} \qquad (6)$$

As shown in the results (Fig. 6), this model captures radial distortions almost perfectly. Still, a slight tangential error, which increases with the distance to the center of distortion, remains. Next, we therefore take these tangential distortion components into account as well.

Radial and Tangential Model

The mathematical description of lateral chromatic variation of the distortion in [17] has been expanded by an extra first order term for the additional lateral color distortion by [16] and is given by the following equations:

$$\begin{aligned}
\Delta \mathbf{e}_c^{rtm}(\mathbf{p}_r) &= \hat{\mathbf{p}}_c^{rtm} - \mathbf{p}_r \\
&= \begin{pmatrix} \Delta e_{c,x}^{rtm}(\mathbf{p}_r) \\ \Delta e_{c,y}^{rtm}(\mathbf{p}_r) \end{pmatrix}
\end{aligned} \qquad (7)$$

$$\begin{aligned}
\Delta e_{c,x}^{rtm}(\mathbf{p}_r) &= n_{c,1} x_r + n_{c,2} x_r r_r^2 + n_{c,3}(3x_r^2 + y_r^2) \\
&\quad + 2n_{c,4} x_r y_r \\
\Delta e_{c,y}^{rtm}(\mathbf{p}_r) &= n_{c,1} y_r + n_{c,2} y_r r_r^2 + 2n_{c,3} x_r y_r \\
&\quad + n_{c,4}(x_r^2 + 3y_r^2)
\end{aligned} \qquad (8)$$

where $\hat{\mathbf{p}}_c^{rtm}$ is the estimate of the image point of the current color channel by this model and $\mathbf{p}_r$ is the image point of the reference color channel. In Eq. (8), $n_{c,1}$ reflects the linear dependency of the refraction index of a lens on the wavelength within the visible spectrum [20], and $n_{c,2}$, $n_{c,3}$ and $n_{c,4}$ are parameters of primary optical aberrations (spherical aberrations and coma) [2]. To each color channel c correspond different parameters $n_{c,i}$, $i = 1, \ldots, 4$.

The parameter vector $\hat{\theta}_c^{rtm} = (u_0, v_0, n_{c,1}, n_{c,2}, n_{c,3}, n_{c,4})^T$ is calculated by solving a nonlinear least squares problem where

the model error, i.e., the difference between the estimated and the measured chromatic aberrations, has to be minimized with the cost function $\|\Delta \mathbf{e}_c^{rtm}(\mathbf{p}_r) - (\mathbf{p}_c - \mathbf{p}_r)\|^2$. A Gauss-Newton method is used to find the solution. This method finds the solution of the nonlinear least squares problem by solving a sequence of linear least squares problems [21]. The parameter vector is first initialized, e.g., with $\hat{\theta}_c^0 = (640, 512, 0, 0, 0, 0)^T$ for images of the size 1280×1024 pixels. An iteration loop then searches the parameter vector $\hat{\theta}_c^{k+1}$ using the $\hat{\theta}_c^k$ from the previous iteration until it converges: the cost function is linearized near $\hat{\theta}_c^k$ and this linearized function is used as a cost function to find $\hat{\theta}_c^{k+1}$.

The wavelength-dependency of this model is further analyzed in the following subsection.

Radial, Tangential and Wavelength-Dependent Model

The values of the parameters $n_{c,i}$, $i = 1, \ldots, 4$ are displayed as a function of the wavelength λ in Fig. 5 by asterisks. They can be approximated by a third-order polynomial of the wavelengths. The polynomial resulting from this approximation is displayed as a dashed line. Considering the $n_{c,i}$, $i = 1, \ldots, 4$, as functions of the wavelengths is a first step: we now include also the dependency of the parameters on the wavelength in the optimization.
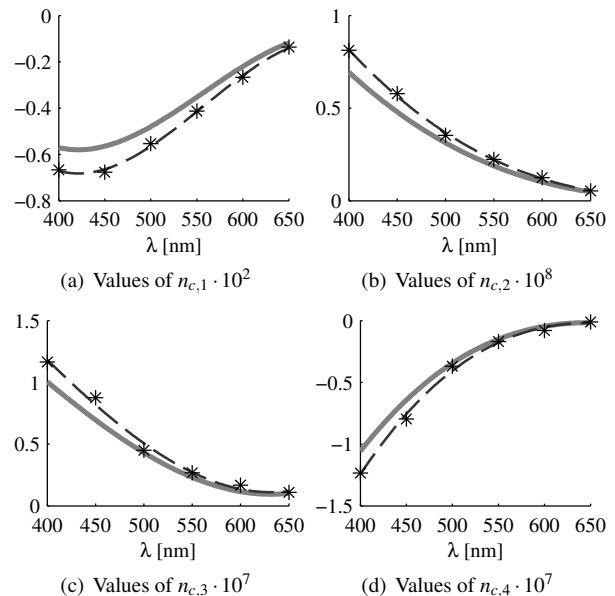

(a) Values of $n_{c,1} \cdot 10^2$

(b) Values of $n_{c,2} \cdot 10^8$

(c) Values of $n_{c,3} \cdot 10^7$

(d) Values of $n_{c,4} \cdot 10^7$

Figure 5. *Comparison of the values of the parameters $n_{c,i}$, $i = 1, \ldots, 4$. The asterisks represent the parameters from the radial and tangential model, the dashed lines are the fittings of these parameters using a third-order polynomial and the solid lines are the results of the radial, tangential and wavelength-dependent model.*

Each parameter $n_{c,i}$, $i = 1, \ldots, 4$ can be replaced by a wavelength-dependent representation in the same way as the parameters $l_{c,i}$ in Eq. (5):

$$n_{c,i} \approx q_{i1} \cdot \lambda_c^3 + q_{i2} \cdot \lambda_c^2 + q_{i3} \cdot \lambda_c + q_{i4}, \qquad (9)$$

where q_{ij}, $j = 1, \ldots, 4$, are the coefficients of the approximation of $n_{c,i}$ by a third-order polynomial.

The coefficients q_{ij} are then included in the previous model of the chromatic aberrations (i.e., the radial and tangential model). The distortions of this new model including the wavelength-dependency are then $\Delta \mathbf{e}^{wl} = (\Delta e_x^{wl}, \Delta e_y^{wl})^T$. The two coordinates of the distortions are defined as follows:

$$
\begin{aligned}
\Delta e_x^{wl}(\lambda, \mathbf{p}_r) &= (q_{11}\lambda^3 + q_{12}\lambda^2 + q_{13}\lambda + q_{14})x_r \\
&+ (q_{21}\lambda^3 + q_{22}\lambda^2 + q_{23}\lambda + q_{24})x_r r_r^2 \\
&+ (q_{31}\lambda^3 + q_{32}\lambda^2 + q_{33}\lambda + q_{34})(3x_r^2 + y_r^2) \\
&+ 2(q_{41}\lambda^3 + q_{42}\lambda^2 + q_{43}\lambda + q_{44})x_r y_r \\
\Delta e_y^{wl}(\lambda, \mathbf{p}_r) &= (q_{11}\lambda^3 + q_{12}\lambda^2 + q_{13}\lambda + q_{14})y_r \\
&+ (q_{21}\lambda^3 + q_{22}\lambda^2 + q_{23}\lambda + q_{24})y_r r_r^2 \\
&+ 2(q_{31}\lambda^3 + q_{32}\lambda^2 + q_{33}\lambda + q_{34})x_r y_r \\
&+ (q_{41}\lambda^3 + q_{42}\lambda^2 + q_{43}\lambda + q_{44})(x_r^2 + 3y_r^2)
\end{aligned}
$$
$$(10)$$

The 16 parameters q_{ij} and the coordinates of the center of the chromatic aberrations $(u_0, v_0)^T$ form the vector $\hat{\theta}^{wl}$ that describes the model of the aberrations over the whole wavelengths range: $\hat{\theta}^{wl} = (u_0, v_0, \{q_{ij}\}_{i=1,\ldots,4, j=1,\ldots,4})^T$.

The parameter vector $\hat{\theta}^{wl}$ can then be calculated like the parameter vector $\hat{\theta}_c^{rtm}$ was in the radial and tangential model, i.e., by minimizing a quadratic cost function using a Gauss-Newton scheme. The difference here is that the cost function takes into account the model errors for all the color channels and not only for one color channel separately. The advantage of this model is that all the parameters are optimized at the same time. The results of this optimization are shown in Fig. 5: the solid lines are the third-order polynomial using the optimized coefficients q_{ij}. The values are quite close to those from the radial and tangential model.

Compensation

After the chromatic aberrations have been characterized with one of the previous models, the compensated images can be computed. The compensation uses the model of the aberrations for the current spectral channel to make it match the reference spectral channel. The compensated image of the current channel has to be equidistantly sampled, therefore we start with the compensated coordinates of the output image that cover all 1280×1024 pixels and go back to the distorted coordinates of the input image. The distorted coordinates can be estimated with $\hat{\mathbf{p}}_c = \mathbf{p}_r + \Delta \mathbf{e}_c$. The pixel values are transferred from the coordinate $\hat{\mathbf{p}}_c$ in the distorted image to the coordinate $\mathbf{p}_r$ in the final compensated image using bilinear interpolation. All the channels - except the reference channel - are processed to complete the compensation of the distortions.

Results

We use a Sony uEye UI2240 CCD camera with a chip size of 7.60 mm $\times$ 6.20 mm and a resolution of 1280×1024 pixels. Our lens is a Tarcus TV Lens 8 mm F1.3. The distance between the checkerboard pattern and the lens is approximately 40 cm. As shown in Fig. 1, the chromatic aberrations result in color fringes on the edges. The distortions between two color channels can be up to 3 pixels (see Fig. 4).

At the beginning of this paper, we explained that placing the spectral bandpass filters between the illumination source and the checkerboard pattern avoids aberrations due to the filters themselves [10]. However, since many paper sheets contain optical brightener, the irradiated light on the paper may be reemitted in a different wavelength range due to fluorescence. This is an issue for color channels close to the ultraviolet like 400 nm. Even the paper we used that was labeled "without any optical brightener" (GMG ProofPaper semimatte 250) was still fluorescent. The results concerning the 400 nm channel must thus be considered carefully.

Dependency on the Wavelengths

In the radial model, for each color channel, the lengths of the distortions are expressed as a function of the distance to the distortion center in the reference color channel (see Fig. 4). It is possible to approximate these lengths by a third-order polynomial of the radius and the coefficients of Eq. (4) are shown in Tab. 1. The coefficients $l_{c,i}$ regarded as functions of the wavelength can in their turn be approximated by a third-order polynomial of the wavelength. The radial model, which only uses the approximated lengths of the distortion and assumes that the distortion is radial, can thus be integrated into a global model, which models the distortions as a function of *both* the wavelength *and* the distance to the distortion center, as defined in Eq. (6). Figure 6 shows the error vectors of the radial model: they all have a direction perpendicular to the line joining the crossings to the center of the distortions. The errors of the radial model are thus only tangential.

Table 1. Coefficients of Eq. (4).

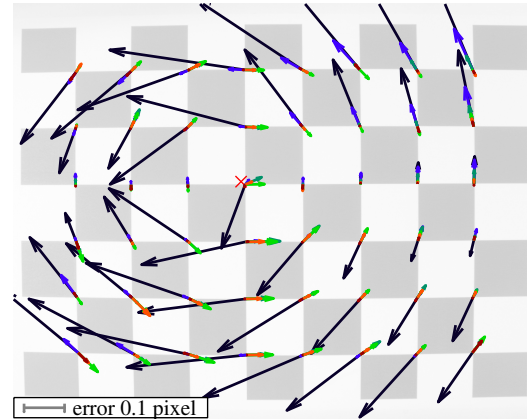| channel c	$l_{c,1} \cdot 10^9$	$l_{c,2} \cdot 10^6$	$l_{c,3} \cdot 10^3$	$l_{c,4} \cdot 10^2$
450 nm	-7.080	2.143	5.762	13.50
500 nm	-4.939	1.846	4.752	10.42
550 nm	-3.581	1.616	3.495	8.023
600 nm	-2.388	1.323	2.177	5.983
650 nm	-1.163	0.7001	1.105	3.365

Figure 6. *The errors of the radial model have tangential components. The center of the image is marked by a red cross. The errors are displayed with a 1000 $\times$ magnification and the colors coding the wavelength bands are the same as in Fig. 3.*

The radial and tangential model exhibits parameters $n_{c,i}$, $i = 1, \ldots, 4$, with a strong wavelength-dependency, as shown in Fig. 5. The first step was to consider the fitted parameters, i.e., the values situated on the dashed line of this figure instead of the values marked by the asterisks. This did not lead to more errors in the model.

The next step was to directly include the coefficients q_{ij} of the approximation of the parameters $n_{c,i}$ with $q_{i1}\lambda_c^3 + q_{i2}\lambda_c^2 + q_{i3}\lambda_c + q_{i4}$ in the optimization. This model including the wavelength-dependency led to almost the same errors and therefore confirmed the validity of the idea of wavelength-dependency of the model. The resulting fittings of the parameters $n_{c,i}$, $i = 1, \ldots, 4$ are given in Tab. 2.

Table 2. Approximation of the parameters $n_{c,i}$, $i = 1, \ldots, 4$, using third-order polynomials.

$$n_{c,1} = -4.893 \cdot 10^{-10} \cdot \lambda^3 + 8.186 \cdot 10^{-7} \cdot \lambda^2 \\ -4.293 \cdot 10^{-4} \cdot \lambda + 6.635 \cdot 10^{-2}$$

$$n_{c,2} = -6.634 \cdot 10^{-17} \cdot \lambda^3 + 1.848 \cdot 10^{-13} \cdot \lambda^2 \\ -1.640 \cdot 10^{-10} \cdot \lambda + 4.721 \cdot 10^{-8}$$

$$n_{c,3} = 2.561 \cdot 10^{-15} \cdot \lambda^3 + -2.545 \cdot 10^{-12} \cdot \lambda^2 \\ +1.542 \cdot 10^{-10} \cdot \lambda + 2.822 \cdot 10^{-7}$$

$$n_{c,4} = 1.868 \cdot 10^{-15} \cdot \lambda^3 - 4.876 \cdot 10^{-12} \cdot \lambda^2 \\ +3.962 \cdot 10^{-9} \cdot \lambda - 1.030 \cdot 10^{-6}$$

Accuracy of the Models

After these results concerning the relation between parameters of the models and the wavelength of a color channel, we show the accuracy of the four presented models in three different ways.

The errors of the estimated distortions are $\|\Delta \mathbf{e}_c(\mathbf{p}_r) - (\mathbf{p}_c - \mathbf{p}_r)\|$, i.e., the difference between the estimated chromatic aberrations $\Delta \mathbf{e}_c(\mathbf{p}_r)$ and the measured chromatic aberrations $\mathbf{p}_c - \mathbf{p}_r$. They are calculated for all crossings contained in the image. In that way, we obtain the mean and maximum errors for each color channel. These errors are displayed in Fig. 7. We can see that the affine model is the least precise one, since its mean and maximum errors are always way above the errors of the other models. Its maximum error is even above 0.2 pixels for the 450 nm, 500 nm and 550 nm channels. For this reason, the wavelength-dependency of the coefficients of the matrix $\mathbf{T}_c$ from the affine model was not analyzed further. The mean errors of the three other models lie below 0.054 pixels and their maximum errors lie below 0.134 pixels (respectively 0.038 and 0.088 pixels if we do not consider the purely radial model).
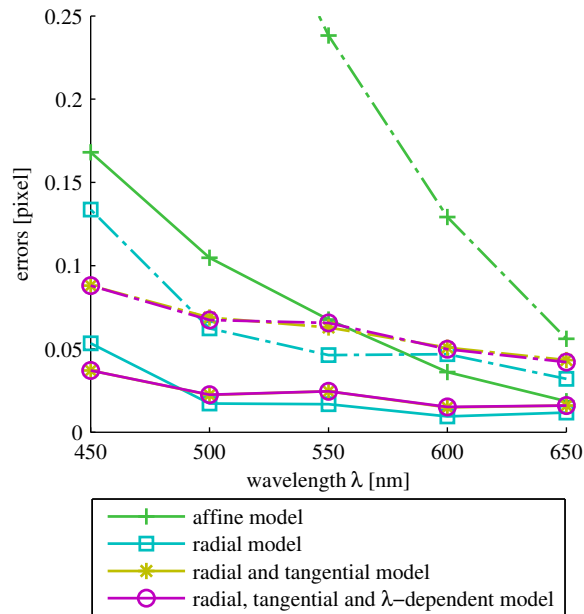

Figure 7. *Errors of the estimated distortions for the presented models: the solid lines represent the mean errors and the dashed lines the maximum errors.*

The accuracy of the models can also be evaluated by the

RGB images that are produced by the combination of the different color channels, like Fig. 1. Color fringes are clearly visible at sharp transitions between white and blacks regions in the image. They are due to poor compensation of the chromatic aberrations on the separate color channels before the combination. Color fringes are also visible on the left column of Fig. 8. The transitions between white and black squares are colored with large orange and blue fringes when the chromatic aberrations are not compensated (Fig. 8(a)). Our results show that the affine model is not adequate for the chromatic aberrations, since green and purple color fringes are still clearly visible in Fig. 8(b). The three other models (i.e., the radial model, the radial and tangential model and the model including the wavelength-dependency) present quite similar accuracy with practically no color fringes in Fig. 8(c).
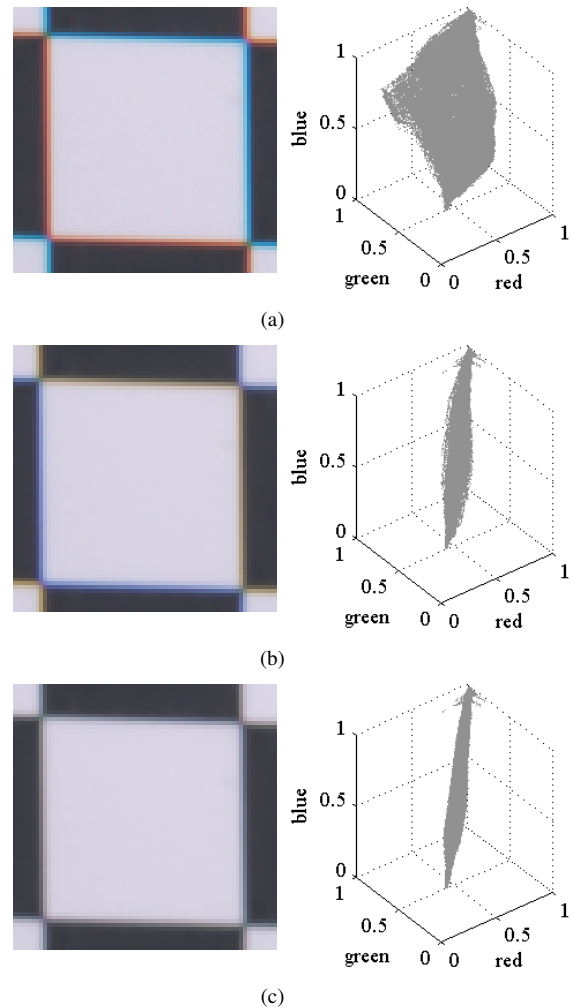

Figure 8. *Visualization of the chromatic aberrations in the original image (a) and their correction with an affine model (b) and with the radial, tangential and wavelength-dependent model (c). The results of the radial model and of the radial and tangential model are similar to the result (c). The left column shows a part of the checkerboard pattern where color fringes can be seen, the right column shows the histograms of the RGB images.*

The color fringes can also be evaluated in histograms of the RGB images. Since we acquired a pattern with only black and white tiles, we would expect all color values to lie on the gray line, which is the diagonal joining the points $(0,0,0)^T$ and $(1,1,1)^T$ in the RGB space. However, because of the chromatic aberrations, the values are spread far from this diagonal. The

right column of Fig. 8 shows the histograms of the RGB images. Without any compensation of the aberrations, the values are far from being only gray (Fig. 8(a)). After utilization of the affine model, the values are closer to the diagonal (Fig. 8(b)). The values closest to gray values are showed in Fig. 8(c): they are obtained with the three other models.

Conclusion

We have measured the chromatic aberrations for different wavelength bands by illuminating a checkerboard pattern with a narrowband light source at different wavelength bands. For our camera system, the image position displacements between two spectral bands are up to 3 pixels. We investigated the chromatic aberrations with several existing models and analyzed the wavelength-dependency of the model parameters. We showed that the parameters can be modeled by a third-order polynomial with respect to the wavelength. We furthermore extended an existing model to include a wavelength-dependency: the model computes the image displacement due to chromatic aberration as a function of the wavelength and the image position and its parameters are jointly optimized. The maximum error of this model lies below 0.088 pixel – when a compensation of images including chromatic aberration is performed, practically no visible artifacts remain after applying the algorithm.

Acknowledgments

References

[1] C. C. Slama, C. Theurer, and S. W. Henriksen. *Manual of Photogrammetry*. American Society of Photogrammetry, Falls Church, VA, 4th edition, 1980.

[2] J. C. Wyant and K. Creath. Basic Wavefront Aberration Theory for Optical Metrology. In R. R. Shannon & J. C. Wyant, editor, *Applied Optics and Optical Engineering*, volume 11, pages 1–53, 1992.

[3] J. Brauers, N. Schulte, A. A. Bell, and T. Aach. Multispectral high dynamic range imaging. In *IS&T/SPIE Electronic Imaging*, pages 680704–1–680704–12, San Jose, California, USA, January 2008.

[4] P. D. Burns and R. S. Berns. Analysis multispectral image capture. In *IS&T Color Imaging Conference*, volume 4, pages 19–22, Springfield, VA, USA, 1996.

[5] H. Haneishi, T. Iwanami, T. Honma, N. Tsumura, and Y. Miyake. Goniospectral imaging of three-dimensional objects. *Journal of Imaging Science and Technology*, 45(5):451–456, 2001.

[6] S. Helling, E. Seidel, and W. Biehlig. Algorithms for spectral color stimulus reconstruction with a seven-channel multispectral camera. In *IS&Ts Proc. 2nd European Conference on Color in Graphics, Imaging and Vision CGIV 2004*, volume 2, pages 254–258, Aachen, Germany, April 2004.

[7] A. Mansouri, F. S. Marzani, J. Y. Hardeberg, and P. Gouton. Optical calibration of a multispectral imaging system based on interference filters. *SPIE Optical Engineering*, 44(2):027004.1–027004.12, February 2005.

[8] A. Ribés, F. Schmitt, R. Pillay, and C. Lahanier. Calibration and spectral reconstruction for crisatel: An art painting multispectral acquisition system. *Journal of Imaging Science and Technology*, 49(6):563–573, November / December 2005.

[9] S. Tominaga. Spectral imaging by a multi-channel camera. *Journal of Electronic Imaging*, 8(4):332–341, October 1999.

[10] J. Brauers, N. Schulte, and T. Aach. Multispectral filter-wheel cameras: geometric distortion model and compensation algorithms. *IEEE Transactions on Image Processing*, 17(12):2368–2380, December 2008.

[11] P. Urban, M. R. Rosen, and R. S. Berns. Spectral image reconstruction using an edge preserving spatio-spectral Wiener estimation. *J. Opt. Soc. Am. A*, 26(8):1865–1875, August 2009.

[12] M. Kozubek and P. Matula. An efficient algorithm for measurement and correction of chromatic aberrations in fluorescence microscopy. *Journal of Microscopy*, 200(3):206–217, December 2000.

[13] T.E. Boult and G. Wolberg. Correcting chromatic aberrations using image warping. In *IEEE Computer Society Conference on Computer Vision and Pattern Recognition*, pages 684–687, Urbana-Champaign, Illinois, USA, June 1992.

[14] N. Joshi, R. Szeliski, and D. J. Kriegman. PSF estimation using sharp edge prediction. In *IEEE Conference on Computer Vision and Pattern Recognition*, pages 1–8, Anchorage, Alaska, June 2008.

[15] R. Willson. Modeling and calibration of automated zoom lenses. In *Proceedings of the SPIE 2350: Videometrics III*, pages 170 – 186, October 1994.

[16] J. Mallon and P. F. Whelan. Calibration and removal of lateral chromatic abberation in images. *Pattern Recognition Letters*, 28:125–135, 2007.

[17] D. C. Brown. Close-range camera calibration. *Photogrammetric Engineering*, 37(8):855–866, January 1971.

[18] W. J. Smith. *Modern Optical Engineering. The Design of Optical Systems*. McGraw-Hill, 3rd edition, 2000.

[19] M. Mühlich and T. Aach. High accuracy feature detection for camera calibration: A multi-steerable approach. In *DAGM07: 29th Annual Symposium of the German Association for Pattern Recognition*, LNCS, pages 284–292, Heidelberg, Germany, September 2007. Springer.

[20] R. Kingslake. *Lens Design Fundamentals*. Academic Press, 1978.

[21] P. Deuflhard. *Newton Methods for Nonlinear Problems. Affine Invariance and Adaptive Algorithms*. Springer, Springer Series in Computational Mathematics, 2nd edition, 2006.

Author Biography

Julie Klein received her diploma degree in electrical engineering and information technology from the Technische Universität München, Germany, and her engineering diploma degree from the Ecole Centrale Marseille, France, in 2008. Since then, she has been working at the Institute of Imaging and Computer Vision, RWTH Aachen University, as a Ph.D. student. Her work focuses on multispectral imaging, in particular the analysis and the compensation of aberrations in multispectral cameras.

Johannes Brauers received his diploma degree in electrical engineering from RWTH Aachen University, Germany, in 2005. Since then he is with the Institute of Imaging and Computer Vision, RWTH Aachen University as a Ph.D. student. His current research interests are multispectral imaging, in particular modeling and compensation of geometric distortions, high dynamic range imaging and identification of the camera transfer function. He received the "EADS Defence Eletronics ARGUS Award 2005" for his master thesis.

Til Aach is Head of the Institute of Imaging and Computer Vision, RWTH Aachen University. From 1993 to 1998, he was with Philips Research Laboratories. From 1998 to 2004, he was a Full Professor and Director of the Institute for Signal Processing, University of Lübeck, Germany. His research interests are in medical and industrial image processing, signal processing, pattern recognition, and computer vision. He has authored or co-authored over 200 papers, and is a co-inventor for about 20 patents.